ICE GENESIS: Synergetic Aircraft and Ground-Based Remote Sensing and In Situ Measurements of Snowfall Microphysical Properties

Anne-Claire Billault-Roux, Jacopo Grazioli, Julien Delanoë, Susana Jorquera, Nicolas Pauwels, Nicolas Viltard, Audrey Martini, Vincent Mariage, Christophe Le Gac, Christophe Caudoux, et al.

BAMS Article

ICE GENESIS

Synergetic Aircraft and Ground-Based Remote Sensing and In Situ Measurements of Snowfall Microphysical Properties

Anne-Claire Billault-Roux, Jacopo Grazioli, Julien Delanoë, Susana Jorquera, Nicolas Pauwels, Nicolas Viltard, Audrey Martini, Vincent Mariage, Christophe Le Gac, Christophe Caudoux, Clémantyne Aubry, Fabrice Bertrand, Alfons Schwarzenboeck, Louis Jaffeux, Pierre Coutris, Guy Febvre, Jean Marc Pichon, Fabien Dezitter, Josué Gehring, Aude Untersee, Christophe Calas, Jordi Figueras i Ventura, Benoit Vie, Adrien Peyrat, Valentin Curat, Simon Rebouissoux, and Alexis Berne

ABSTRACT: An international field experiment took place in the Swiss Jura in January 2021 as a milestone of the European ICE GENESIS project (www.ice-genesis.eu/), which aims to better measure, understand, and model the ice/snow particle properties and mechanisms responsible for icing of rotor-craft and aircraft. The field campaign was designed to collect observations of clouds and snowfall at a prescribed range of temperatures (–10° to +2°C). The suite of in situ and remote sensing instruments included airborne probes and imagers on board a SAFIRE ATR-42 aircraft, able to sample liquid and ice particles from the micron to the millimeter size range, as well as icing sensors and cameras. Two 95 GHz Doppler cloud radars were installed on the SAFIRE ATR-42, while six Doppler weather radars operating at frequencies ranging from 10 to 95 GHz (and one lidar) were ground based. An operational polarimetric weather radar in nearby France (Montancy) complements the coverage. Finally, observations of standard meteorological variables as well as high-resolution pictures of falling snowflakes from a multiangle snowflake camera were collected at the ground level. The campaign showed its full potential during five (multihourly) flights where precipitation was monitored from cloud to ground. The originality of this campaign resides in the targeted specific temperature range for snowfall and in the synchronization between the ground-based remote sensing and the aircraft trajectories designed to maximize the collection of in situ observations within the column above the radar systems.

KEYWORDS: Precipitation; Cloud microphysics; Icing; Snowfall; Radars/Radar observations; Remote sensing

https://doi.org/10.1175/BAMS-D-21-0184.1
Corresponding author: Jacopo Grazioli, jacopo.grazioli@epfl.ch
In final form 27 October 2022

AFFILIATIONS: Billault-Roux,* Grazioli,* and Berne—Environmental Remote Sensing Laboratory, École Polytechnique Fédérale de Lausanne, Lausanne, Switzerland; **Delanoë, Jorquera, Pauwels, Viltard, Martini, Mariage, Le Gac, Caudoux, and Bertrand**—Laboratoire Atmosphère, Milieux et Observations Spatiales, IPSL, UVSQ Université Paris-Saclay, Sorbonne Université, CNRS, Guyancourt, France; **Aubry**—Laboratoire Atmosphère, Milieux et Observations Spatiales, IPSL, UVSQ Université Paris-Saclay, Sorbonne Université, CNRS, Guyancourt, France, and Deutsches Zentrum für Luft- und Raumfahrt, Institut für Physik der Atmosphäre, Oberpfaffenhofen, Germany; **Schwarzenboeck, Jaffeux, Coutris, Febvre, and Pichon**—Laboratoire de Météorologie Physique, Aubière, France; **Dezitter**—Airbus Helicopters, Marignane, France; **Gehring and Untersee**—Federal Office of Meteorology and Climatology (MeteoSwiss), Geneva, Switzerland; **Calas, Figueras i Ventura, Vie, Peyrat, Curat, and Rebouissoux**—Météo-France, Toulouse, France

* Equal contribution to this work by the first two authors.

The aviation industry faces numerous safety-related challenges in cold atmospheric conditions. The risk of aircraft icing in supercooled or mixed-phase clouds is a well-known example (Cao et al. 2018). Likewise, ice crystal icing, often associated with flying in high-altitude regions near deep convective systems (Lawson et al. 1998; Hallett and Isaac 2008), leads to the ingestion of ice crystals by jet engines and subsequent power loss or engine damage (Mason et al. 2006; Haggerty et al. 2019).

Snowfall has also been reported to induce in-flight power interruptions on certain engines, while at ground level, snow accretion on aircraft is an additional threat for takeoff (Rasmussen et al. 1999, 2000, 2001; Taszarek et al. 2020). To comply with certification requirements addressing these risks, aircraft and helicopter manufacturers need to substantiate that each engine and its air inlet system can safely operate in snow, both falling and blowing, without adverse effect on engine operation. The available regulatory and guidance documents define approximations of conditions to be tested: concerning snowfall and blowing snow, the Federal Aviation Administration (FAA) in the Advisory Circular AC29-2C and Acceptable Means of Compliance AMC25.1093 prescribes temperature conditions between −9° and +2°C. However, there are no validated engineering tools (test facilities and numerical tools) available to support the design of air inlet systems by assessing the risk of snow accretion or accumulation within this prescribed temperature range. Demonstration is thus performed at the end of the program development during certification flights, and any issue found at this stage of the development can lead to significant delays and costs. To secure future program development and certification, there is a need to better characterize the microphysical properties of snowfall for individual particles or particle populations (number, mass, mass–size relation, fractal dimension, density, sphericity, and ice water content, to list a few) to support the development of engineering tools and de-risk design before in-flight demonstration.

The measurement efforts presented in this paper are tailored to provide observations of snowfall properties at this temperature range, slightly extended to [−10, +2]°C, with the primary motivation to cover this important industrial need. This work is a specific contribution to the work package 5 (WP5) of the international project ICE GENESIS (www.ice-genesis.eu/). Within WP5, the main objective is to quantify the microphysical properties of snow crystal populations during snowfall; these data will then serve to specify snow properties to be generated in icing wind tunnels (WP7) and simulated in numerical tools (WP10). We highlight

here that the primary focus of this project is related to snowfall conditions, rather than icing due to supercooled liquid water droplets.

Different precipitation and heat transfer processes take place between −10° and +2°C, depending on the population of ice particles, relative humidity, and availability of supercooled liquid water (Stewart et al. 2015). Their proper understanding and characterization is a challenge beyond aircraft industrial concerns, in particular for the development of more accurate numerical weather and climate models (Grabowski et al. 2019; Morrison et al. 2020).

Among the processes leading to particle growth, aggregation is maximized between −5° and 0°C (Pruppacher and Klett 2010; Heymsfield et al. 2015) due to the particles' increased sticking efficiency. Secondary ice production is also known to take place in this temperature range through various mechanisms, including rime splintering (Hallet and Mossop 1974; between −8° and −3°C), collisional breakup (e.g., Ramelli et al. 2021), or droplet shattering during freezing (e.g., Korolev et al. 2020); these are among the still poorly represented processes in numerical weather models, and have been the subject of strong renewed interest in the past decade (e.g., Field et al. 2016; Korolev and Leisner 2020).

Transitioning to warmer temperatures, processes occurring slightly above and within the melting layer can have sizable socioeconomical repercussions. Two examples are snow buildup on power lines (e.g., Poots 2000), or signal deterioration in telecommunications (e.g., Bellon et al. 1997). They are also a known concern for remote sensing estimation of precipitation, which can be biased by the melting layer's brightband signature in weather radar data, and by the attenuation it further induces (e.g., Szyrmer and Zawadzki 1999; Leinonen and von Lerber 2018, and references therein). The actual importance and quantification of aggregation and breakup, of changes in shape and bulk density, across the melting layer, are important and debated questions (Fabry 1995; Li and Moisseev 2019). Although recent progress in modeling has helped gain insight in particle-scale melting mechanisms [Szyrmer and Zawadzki (1999) and more recently Leinonen and von Lerber (2018)], a gap remains to be filled to fully comprehend the interplay of microphysical, thermodynamical, and aerodynamical processes in wet snow (Li et al. 2020).

Current knowledge about processes occurring near the melting layer consists of indirect weather radar observations (e.g., Liao et al. 2009; Trömel et al. 2019; Li and Moisseev 2020) and to a minor extent of direct measurements collected by instrumented aircraft (Heymsfield et al. 2015), ground-based in situ observations (Knight 1979; Barthazy et al. 1998), laboratory studies (Mitra et al. 1990; Oraltay and Hallett 2005; Hauk et al. 2016; Aguilar et al. 2021), and simulations (Leinonen and von Lerber 2018). ICE GENESIS, with its multiple work packages, recognizes that it is crucial to act on all these fields. It will contribute to better understand these processes thanks to the coordinated collection of high-quality data from both remote sensing and in situ measurements and to the reproduction and modeling of associated physical phenomena like drag or melting.

The ICE GENESIS WP5 campaign is a multisensor experiment featuring ground-based and airborne remote sensing and in situ measurements during a 2-week timeframe in January 2021. The added value of airborne radars on board aircraft equipped with in situ sampling instruments has been documented (Protat et al. 2007; Wang et al. 2012; Houze et al. 2017), as well as the synergy between ground-based weather radars and airborne instruments (Bousquet et al. 2015; Murphy et al. 2020). As detailed in the next section, we consistently aimed to collect in situ data of precipitation in a predefined temperature range near the melting layer and at the same time sample the entire column of precipitation *from cloud to ground* with different remote sensing instruments. The setup was specifically designed to optimize the collocation of the various sensors by ensuring sequential aircraft overpasses over the

ground site, between higher altitudes corresponding to the −10°C temperature level down to lower altitudes at maximum +2°C.

Other campaigns with similar setups featuring ground-based and airborne sensors have fostered the improvement of precipitation quantification and the development and validation of new retrieval algorithms (e.g., Currier et al. 2017; Leinonen et al. 2018; Chase et al. 2018; Mason et al. 2018). The Olympic Mountains Experiment (OLYMPEX; Houze et al. 2017) was, for instance, designed to study precipitation at the interface between ocean, coastal, and mountainous areas and had a clear target to support and improve satellite-based observations; the Global Precipitation Measurement Cold Season Precipitation Experiment (GCPEX; Skofronick-Jackson et al. 2015) was dedicated to retrieving snowfall processes and properties with the similar aim of improving satellite estimates of precipitation; the Investigation of Microphysics and Precipitation for Atlantic Coast-Threatening Snowstorms (IMPACTS; McMurdie et al. 2022) involved the investigation of snowstorms and the variability of their characteristics across scales (from microphysics to large-scale precipitation patterns); and Biogenic Aerosols—Effects on Clouds and Climate (BAECC; Petäjä et al. 2016) was devoted to the study of clouds and aerosols in Finland.

The novelty of the ICE GENESIS experiment comes from its specific target on snowfall microphysics at mild (and well defined) temperatures, and from the synergy (in terms of collocation, altitudinal range, and high resolution) between remote sensing and in situ instruments. Thanks to those features, the dataset presented here will bring new opportunities to improve the representation of snowfall properties and processes, with scientific applications extending well beyond aircraft design and related industrial challenges.

Experimental setup

Campaign location and sampling strategy. The location of the field campaign was chosen based on practical and climatological constraints. One objective was to maximize chances of observing snowfall at ground level in order to allow the use of in situ instruments and to reduce attenuation issues caused by rainfall for the ground-based weather radars. At the same time, the terrain should allow flights down to relatively low heights above ground to ensure that the airborne measurements sample the appropriate mild temperature range (−10° to +2°C) as close as possible to the ground site. Based on these criteria it was decided to set up the field campaign in the city of La Chaux-de-Fonds in the Swiss Jura, at an altitude of 1,020 m MSL, with on average 28 days of snowfall and 330 mm total precipitation per meteorological winter.[1] The ground-based sites, which included remote sensing and in situ sensors as detailed in the section "Ground-based data sources," were located within and in the near vicinity of the city airport Les Éplatures, i.e., at the valley floor (Fig. 2).

[1] December–February, compiled from MeteoSwiss automatic measurements 1980–2020.

Although this is not the primary focus of the experiment, the location of La Chaux-de-Fonds in complex terrain also opens up the possibility to observe and study orographic-induced precipitation processes: in spite of a relatively modest elevation (max 1,700 m), the Jura mountain range benefits from orographic enhancement of precipitation (Foresti et al. 2018).

The French ATR-42 environmental research aircraft of SAFIRE,[2] whose instrumental payload is described in the section "Aircraft data," was stationed in the closely located Dijon airport (France), 30 min flight time from La Chaux-de-Fonds. Potential flights were identified a few days ahead following a daily weather briefing, jointly conducted by MeteoSwiss and Météo-France. Flight strategies and schedules were then finalized a few hours before the flights on the basis of the latest weather forecast and assessment of flight conditions.

[2] www.safire.fr/en/content_page/safire-utilisateurs/latr42-2.html

The flight plans included relatively short (15–25 km) legs in the vicinity of the ground instruments—with occasional longer (~40 km) legs—following the main direction of the terrain (northeast–southwest) as can be seen on Fig. 1b. The sampling legs were performed at different constant-altitude flight levels as sketched on Fig. 1a, which were chosen depending on the temperature profile and within the authorized flight paths, constrained by the topography. Below the minimum sector altitude (MSA), the aircraft followed approach trajectories as published in IFR (Instrument Flight Rules) charts. The altitude range of each flight is referenced in Table 3. Note that this strategy was preferred to other possible vertical sampling maneuvers (e.g., Lagrangian spiral descent) due to operational and terrain constraints.

This measurement setup in the vicinity of an airport ensured that the aircraft could sample down to low heights (~100 m above ground) while ensuring almost perfect collocation with the ground-based instruments deployed at the airport. This also allowed the aircraft to adjust the altitude of its flight levels in order to sample precisely the target conditions. Given the objective of the campaign, this flexibility is a strong added value in comparison with other experiments relying on instruments deployed at fixed altitudes (e.g., Barthazy et al. 1998).

Ground-based data sources. The main ground measurement site (site 1 of Figs. 1 and 2), within the airport Les Éplatures, comprised a suite of remote sensing instruments: a high-sensitivity X-band Doppler spectral profiler (ROXI; Viltard et al. 2019), a K-band Doppler spectral profiler (MRR-PRO; see, e.g., Loeffler-Mang et al. 1999; Ferrone et al. 2022), a dual-polarization W-band Doppler spectral zenith profiler complemented with an 89 GHz radiometer (WProf; Küchler et al. 2017), an additional W-band profiler (BASTA-mobile; Delanoë et al. 2016), and a scanning system (BALI) composed of a W-band radar (mini-BASTA; Delanoë et al. 2016) and a 808 nm micropulse lidar (SLIM, adapted from Mariage et al. 2017). BALI performed hemispherical scans during aircraft flights, along the direction of the flight track.

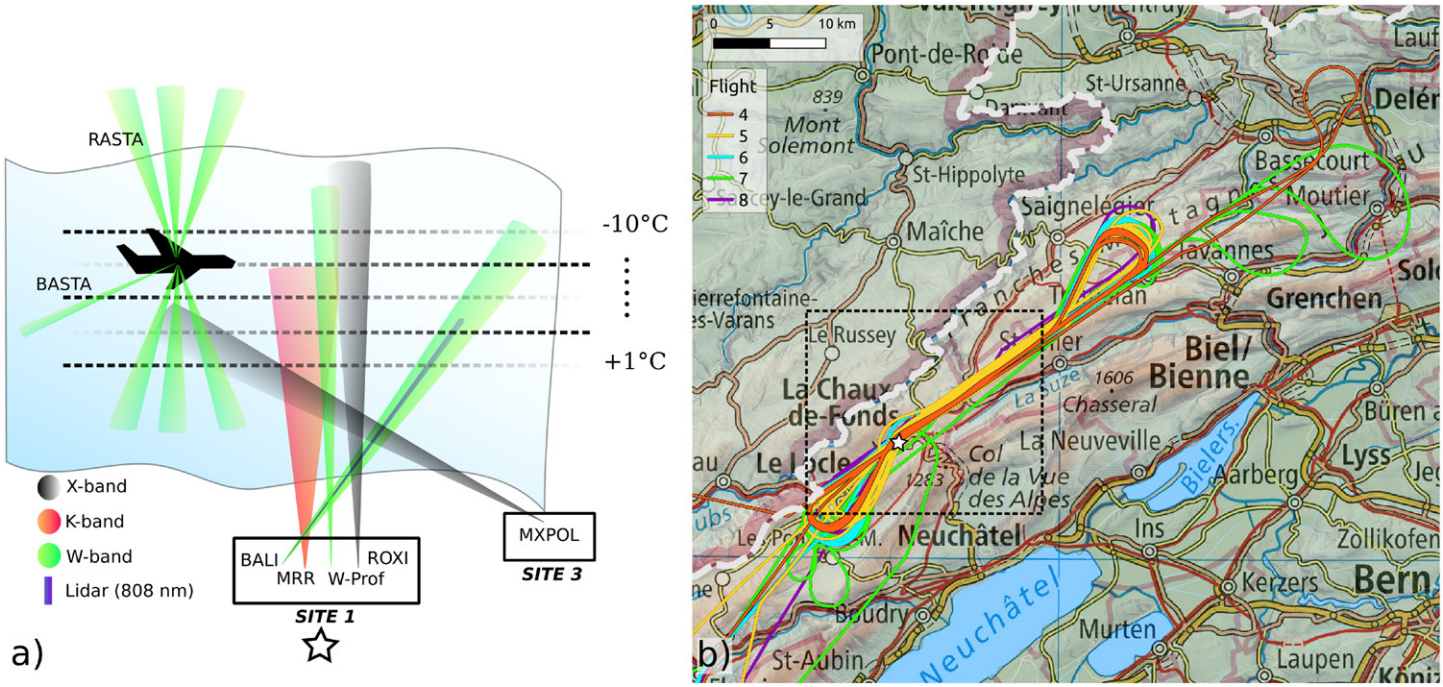

Fig. 1. (a) Schematic illustration of the combination of remote sensing measurements collected during typical flights. (b) GPS trajectories of the aircraft during all flights of the campaign; flights are numbered as in Table 3. The black-dashed rectangle delineates the area shown in Fig. 2, and the white star corresponds to site 1. The light gray dashed line indicates the Swiss–French border. Map: Swiss Map Raster 500 and SwissALTI3D, Federal Office of Topography swisstopo; BDALTI, Institut national de l'information géographique et forestière (IGN-F).

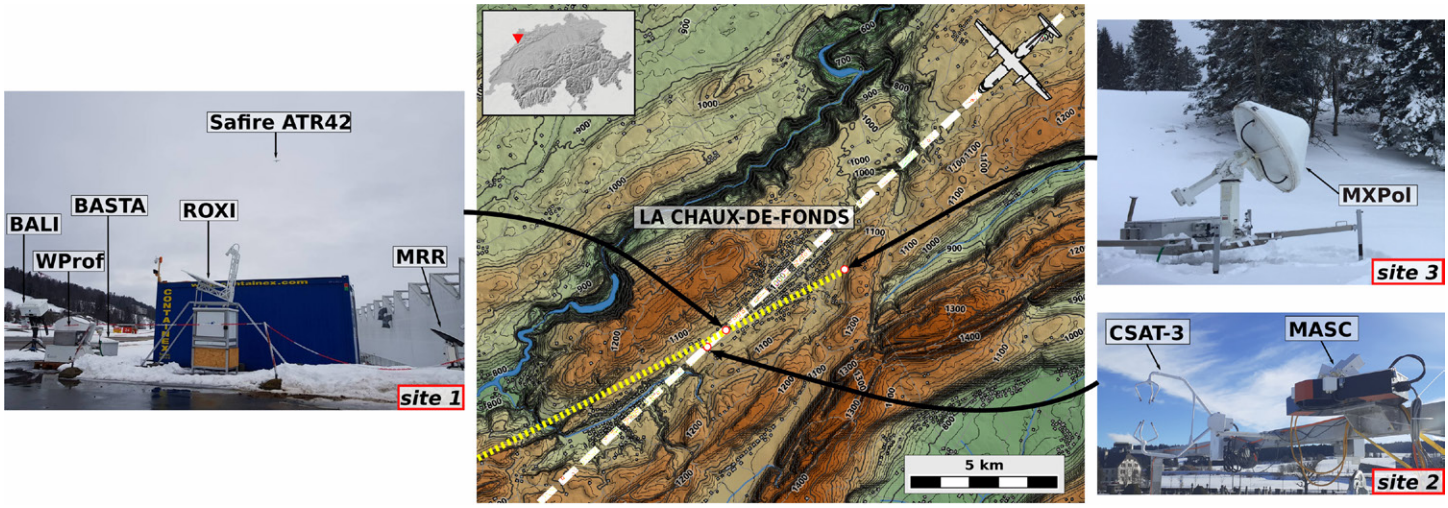

Fig. 2. Map of the locations of the ground-based measurement sites of the field campaign and pictures of the instruments deployed on each site. Acronyms of the instruments are defined in Table 1. Yellow short-dashed line indicates direction of RHI performed by MXPol. A white dashed line shows the approach line of ATR-42 during the overpasses and coincides with direction of hemispherical RHI performed by BALI. The location of the sites is as follows. Site 1: 47.085°N, 6.797°E, 1,019 m MSL. Site 2: 47.083°N, 6.792°E, 1,017 m MSL. Site 3: 47.102°N, 6.856°E, 1,122 m MSL. Montancy: 47.369°N, 7.019°E, 913 m MSL. Map: SwissALTI3D and SwissTLM3D, Federal Office of Topography swisstopo; BDALTI, Institut national de l'information géographique et forestière (IGN-F).

Two secondary sites, site 2 and site 3, completed the setup. Five hundred meters away along the landing track, within the enclosure of an operational weather station of MeteoSwiss (site 2), a Multi-Angle Snowflake Camera (MASC; Garrett et al. 2012; Grazioli et al. 2022) and a sonic anemometer (CSAT-3) were installed. The weather station complements the measurements with standard atmospheric variables as well as precipitation amount and snow height.

Finally, an X-band polarimetric radar (MXPol; e.g., Schneebeli et al. 2013) was deployed 4.8 km away from the airport at site 3 and performed 5-min scanning cycles with four RHI scans in the direction of the main site (site 1) as well as one vertical bird bath PPI scan, for a posteriori differential reflectivity (Z_{DR}) calibration. The setup is summarized in Table 1 and illustrated in the map and pictures in Fig. 2. An operational C-band polarimetric radar of Météo-France, located in Montancy, 36 km to the northeast of La Chaux-de-Fonds, performs routine volume scans at low elevations, thus providing additional large-scale coverage of precipitation systems in the area of interest.

Aircraft data. An instrumental payload was integrated on the aircraft allowing for both in situ measurements and remote sensing of snowfall conditions, as summarized in Table 2 and depicted in Fig. 3. A set of in situ imaging probes (optical array probes) allowed us to observe hydrometeors across the full size spectrum: the 2D-S and CIP probes cover the smaller snow particle sizes, while PIP and HVPS can capture nominal particle sizes up to 6.4 and 19.2 mm, respectively. Measurements of snow bulk properties were performed using hot-wire probes: a ROBUST probe (e.g., Grandin et al. 2014; Strapp et al. 2008), which measures total condensed water content (TWC); a Nevzorov probe, which discriminates between ice and liquid water content; and the LWC-300, which measures LWC only [see, e.g., Baumgardner et al. (2017) and McFarquhar et al. (2017) for a comprehensive reference of the instruments]. The payload also included a counterflow virtual impactor (CVI; Anderson et al. 1994; Schwarzenbo and Heintzenberg 2000) specifically adapted to measure total water content in snowfall conditions with large hydrometeors. Additionally, the CDP-2 scattering probe was installed for droplet size and concentration measurements. A snow accretion monitoring device was specifically conceived for the campaign and integrated on the aircraft. It consists

Table 1. Details of ground sensors deployed during the measurement period and the currently available data. All radar profilers were cross calibrated (details in section "Insights from complementary measurements"), but no attenuation correction was performed at this stage. L2 data refer to files containing at least one variable obtained as output of a retrieval method rather than directly provided by the instrument.

Name	Acronym	Deployment	Measured and retrieved quantities
W-band Doppler profiling cloud radar	WProf	14 Jan–1 Feb	L0: Radar Doppler spectra (dual-polarization); L2: radar moments (reflectivity, mean Doppler velocity, spectrum width, slanted linear depolarization ratio) and estimates of liquid water path and integrated water vapor (Billault-Roux and Berne 2021)
Weather station coupled to WProf	WProf-AWS	14 Jan–1 Feb	Temperature, pressure, relative humidity, wind speed
K-band Doppler profiling radar	MRR-PRO	14 Dec–27 Mar	L0: Radar Doppler spectra; L2: radar moments (reflectivity, mean Doppler velocity, spectrum width), processed following Ferrone et al. (2022)
X-band Doppler profiling radar	ROXI	18 Dec–28 Jan, 18 Feb–27 Mar	L0: Radar Doppler spectra; L1: radar moments (reflectivity, mean Doppler velocity, spectrum width)
W-band profiling radar	BASTA-mobile	18 Dec–27 Mar	L1: Radar moments (reflectivity, mean Doppler velocity)
W-band scanning radar + 808 nm lidar	BALI (mini-BASTA + SLIM)	18 Dec–27 Mar	L1: Radar moments (reflectivity, mean Doppler velocity), lidar backscatter (hemispherical RHIs)
X-band scanning polarimetric radar	MXPol	13 Jan–27 Mar	L0: vertical PPI radar Doppler spectra (dual-polarization); L2: RHIs with radar moments {reflectivity, mean Doppler velocity, Doppler spectrum width, differential reflectivity [calibration with Ferrone and Berne (2021)], correlation coefficient, differential phase shift, specific differential phase (Schneebeli et al. 2014)} and hydrometeor classification with demixing (Besic et al. 2018)
Multiangle snowflake camera	MASC	14 Dec–15 Mar	Grayscale images of snow particles and classification according to hydrometeor type (Praz et al. 2017; Grazioli et al. 2022)
3D sonic anemometer	CSAT3	14 Dec–27 Mar	High-resolution measurements of three-dimensional wind field
MeteoSwiss automatic weather station	MCH-AWS	—	Standard atmospheric parameters, weighing rain gauge, and snow height measurements
Météo-France operational polarimetric radar in Montancy	MTCY	—	PPIs with radar moments (reflectivity, differential reflectivity, specific differential phase, Doppler velocity and spectrum width, correlation coefficient)

of a de-iced cylinder and a dedicated camera to record potential snow accretion during the flights and collect data for subsequent validation of numerical tools within ICE GENESIS.

The aircraft payload also comprised a combination of two multiantenna W-band radars. RASTA (RAdar SysTem Airborne) is a multibeam 95 GHz Doppler spectral cloud radar (Plana-Fattori et al. 2010; Delanoë et al. 2013) with one nadir-looking and three noncolinear upward-looking antennas allowing for the retrieval of the three-dimensional wind field after correction of aircraft motion. BASTA (Bistatic rAdar SysTem for Atmospheric studies; adapted from Delanoë et al. 2016) is a frequency-modulated continuous-wave (FMCW) radar

Table 2. Instrumental configuration of the SAFIRE ATR-42: microphysical probes and remote sensing instruments. Mass-related quantities of ice crystals (ice water content and median mass diameter) are retrieved from imagers (2D-S, CIP, PIP, HVPS) assuming a mass–size relationship (Leroy et al. 2016): these are estimates rather than measurements.

Name	Acronym	Measured and retrieved quantities
Aircraft probes	—	GPS, altitude, pressure, true airspeed, static air temperature, heading
Dewpoint and condensation hygrometers	ACH	Absolute and relative humidity
Cloud droplet probe	CDP-2	Cloud droplet number size distribution (DSD) (range: 3–50 μm), liquid water content, total droplet number concentration, median volume diameter
2D-Stereo	2D-S	Particle size distribution (PSD) (range: 10 μm–1.28 mm), mass–size distribution, total number concentration, median mass diameter, ice water concentration, black-and-white images of ice hydrometeors (some of which captured from two 90°-apart views)
Cloud imaging probe	CIP	PSD (range: 25 μm–1.6 mm), mass–size distribution, total number concentration, median mass diameter, ice water content, black-and-white images
Precipitation imaging probe	PIP	PSD (range: 100 μm–6.4 mm), mass–size distribution, total number concentration, median mass diameter, ice water content, black-and-white images
High-volume precipitation spectrometer	HVPS	PSD (range: 150 μm–1.92 cm), mass–size distribution, median mass diameter, ice water content, black-and-white images
Counterflow virtual impactor	CVI-Snow	Total condensed water content (TWC)
ROBUST WC-3000 hot-wire probe	ROBUST	TWC
Nevzorov hot-wire probe	Nevzorov	TWC, liquid water content (LWC)
LWC-300 hot-wire probe	LWC-300	LWC
Sideward-looking W-band radar	BASTA	L1: radar moments (reflectivity, mean Doppler velocity)
Accretion monitoring device	AccrS	Images of snow accretion on rod
Upward- and downward-looking multiantenna W-band radar	RASTA	L0: Radar Doppler spectra; L2: radar moments (reflectivity, mean Doppler velocity) and retrieved three-dimensional wind field (Bousquet et al. 2016).

sideward-looking 95 GHz Doppler radar, whose purpose is to derive cloud and precipitation properties at the altitude of the aircraft up to 10 km horizontal range, thus complementing the vertical profiles measured by RASTA.

Dataset. The data collected during the experiment cover two nested time frames. The ground-based instruments (see section "Ground-based data sources") have been deployed for a longer period (from mid-December 2020 to the end of March 2021, see Table 1). Within this time

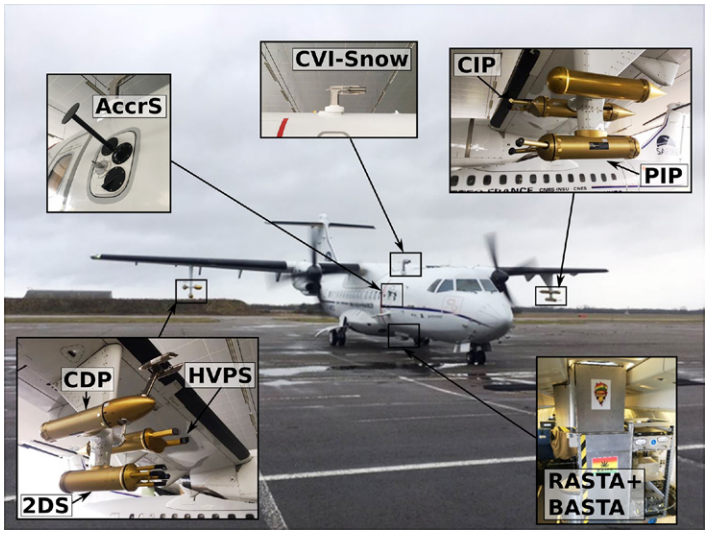

Fig. 3. Picture with details of the instruments deployed on board the SAFIRE ATR-42 aircraft. Acronyms are defined in Table 2.

interval, an enhanced observation period took place during the second half of January when the SAFIRE ATR-42 scientific aircraft joined the continuous ground-based observations, providing the multi-instrument setup illustrated in Fig. 1: the flights took place between 22 and 30 January. Overall, measurements from 14 h of flight (above ground site) were recorded, comprising a total of 100 flight legs. Table 3 summarizes this enhanced observational period, during which the full synergy between in situ and ground-based instruments was achieved. We hereafter focus on this enhanced observational period, as it is the main added value of the measurement setup presented here.

The synoptic situation during this time of the year was dominated by a succession of lows over northwestern Europe, which maintained mostly dynamic and wet conditions over Switzerland after a few dry days (18–21 January). Between 23 and 27 January, the weather was cold enough to bring snowfall at ground level, while the last days of January were characterized by warmer temperatures with rainfall at ground level and a melting layer around 1,500–2,000 m MSL. During this period (22–30 January), 140 mm of total precipitation were recorded and about 120 h of precipitation, of which 70 h were with snowfall at the ground level at the airport site.

Figure 4 summarizes the intense observation period through a selection of ground-based in situ and remote sensing data. The W-band radar data reflect the succession of multiple precipitation systems over La Chaux-de-Fonds, with both shallow and deep cloud layers. These precipitation events were associated with ground temperatures ranging from −6°C at the coldest to +6°C at the warmest. In terms of snowfall microphysical properties, Fig. 4c displays the hydrometeor classification output from MASC images (from Praz et al. 2017): the snow particle populations captured by the MASC were dominated by graupel-like and aggregate particles apart from small particles.[3] The apparent melting proportion, estimated from MASC images together with the hydrometeor types, correlates rather well with the measured ground temperatures, i.e., higher melting-particle proportions are identified at time steps with temperatures slightly above 0°C.

[3] A hydrometeor class used for all the hydrometeors too small to be reliably assigned to a given class.

From an aircraft perspective, diverse snowfall conditions and microphysical properties were sampled during the five flights, as illustrated in Table 3 and Fig. 5. In terms of snow habit, rimed aggregates and more fragile aggregates were the dominant particle types

Table 3. Summary of flight data during the enhanced observation period of January 2021. Times indicate takeoff and landing. The temperature range sampled by the aircraft during the legs is included.

Flight reference, time, and date	Synoptic situation	No. of legs	Altitude range of legs: min–max (m MSL)	Temperature range: min–max (°C)
F04: 1340–1720 UTC 22 Jan	Cold front approaching from the northwest associated with a trough extending from Norway to southern France	18	1,310–3,214	−8.1 to +2.8
F05: 1230–1630 UTC 23 Jan	Postfrontal showers activated by a short-wave trough	22	1,238–2,706	−12.5 to +1.7
F06: 1330–1700 UTC 27 Jan	Behind a trough extending from Norway to Greece; passage of a jet streak in a northwesterly flow	18	1,244–3,329	−9.1 to +0.47
F07: 0850–1205 UTC 28 Jan	Passage of a warm front associated with a low over the North Atlantic	14	1,811–3,300	−9.0 to +2.3
F08: 1030–1530 UTC 30 Jan	Passage of a cold front and a short-wave trough associated with a low over the Celtic Sea	28	1,511–3,660	−9.3 to +1.6

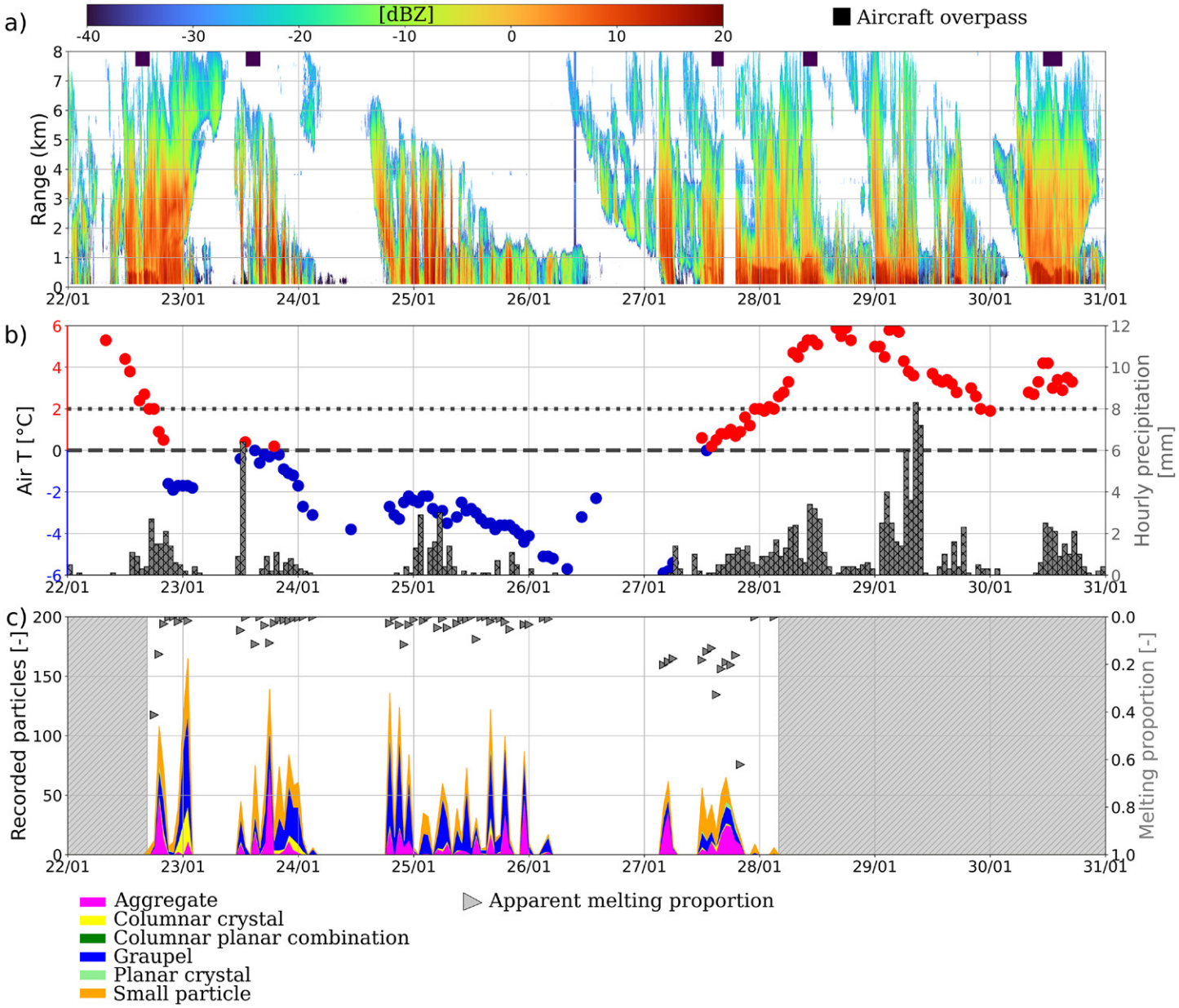

Fig. 4. Overview of the enhanced observation period (measurements including aircraft overpasses). (a) Time–height structure of reflectivity from the vertically pointing W-band profiler (WProf). (b) Average hourly temperature at ground level (only during precipitation) color coded for positive and negative temperatures; bar plot (right *y* axis) shows hourly precipitation (source: MeteoSwiss). (c) Time evolution of hydrometeor types recorded by the MASC near ground level and average proportion of particles showing melting morphology (MASC data averaged over 1 h consecutive intervals). Only MASC data collected at temperatures lower than 2°C are shown and hourly time intervals with at least five particles recorded. Hatched areas correspond to time intervals with temperatures higher than 2°C.

identified in PIP images (Jaffeux et al. 2022), followed by columnar crystals and graupel. The hydrometeor classification from the airborne 2D-S (Jaffeux et al. 2022; shown in Fig. 5c) reveals microphysical properties and processes at small scale ($D_{max} \leq 1{,}280$ μm, i.e., which typically excludes aggregates) and can thus help identify regions where ice production (primary or secondary) is occurring.

Data showcase: 27 January flight

In this section we will focus, as a showcase, on the flight taking place on 27 January, which, as we shall see, was well representative of the ICE GENESIS target conditions.

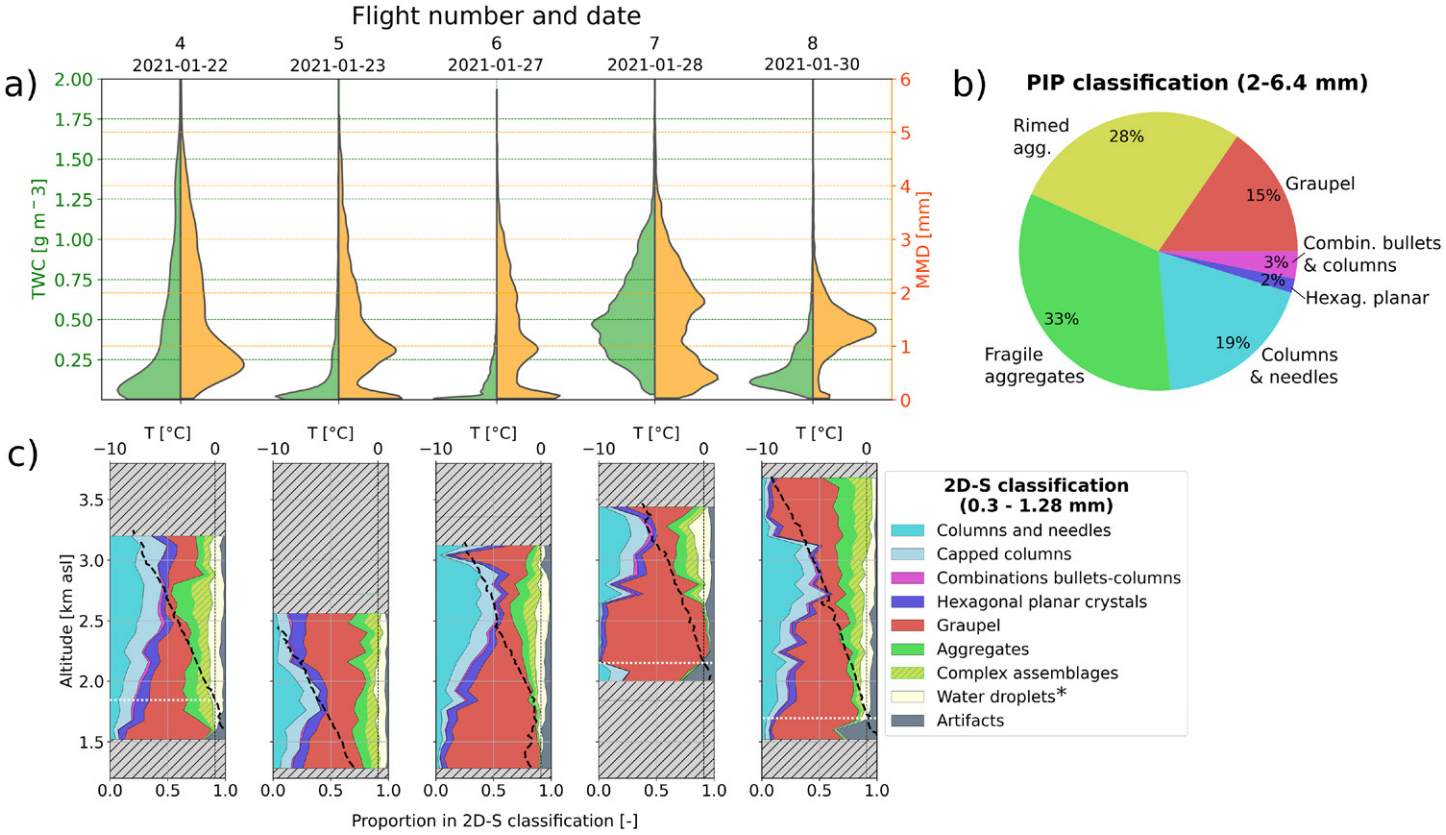

Fig. 5. (a) "Violin plots" (i.e., featuring a kernel density estimation of the underlying distribution) of the TWC (CVI measurement) and median mass diameter (MMD, calculated from 2D-S and PIP; Leroy et al. 2016) for the different flights. (b) Hydrometeor classification from PIP images (size range: ~2–6.4 mm; Jaffeux et al. 2022), all flights merged. (c) Proportion of hydrometeor types in 2D-S images as a function of altitude, during each flight (size range: ~300–1,280 μm; Jaffeux et al. 2022), with mean temperature profile measured by the aircraft. Note that the morphological classes are slightly different between the two probes. White line shows where mean temperature profiles cross 0°, a rough indicator of the start of the melting layer, below which the classification is less reliable. Out-of-focus water droplets are still classified as such, but their size can be overestimated (e.g., Vaillant De Guélis et al. 2019); this class therefore also includes droplets *smaller* than 300 μm, e.g., cloud droplets.

Synoptic and observational overview. At 1200 UTC 27 January 2021, La Chaux-de-Fonds was located on the rear side of a trough directing a strong northwesterly flow over Switzerland (Fig. 6b). A warm front associated with a deep low pressure system over the North Atlantic (Fig. 6a) led to stratiform precipitation with an increase of the snowfall line from ground level to about 2,000 m MSL. This synoptic event brought a total of 35 mm of precipitation at the measurement site (from 0300 UTC 27 January to 1500 UTC 28 January), with a transition from the solid to the liquid phase around 2100 UTC.

Flight overpasses of the ATR-42 occurred between 1400 and 1600 UTC, with 18 flight legs performed between 1300 and 3300 m MSL, i.e., between 280 and 2300 m above ground. The TWC was up to 0.54 g m^{-3} (Table 3), and the temperature of the airborne measurements ranged from −9° to +1°C (cf. mean temperature profile in Fig. 5 and its temporal evolution in Fig. A1 in the appendix). At the same time, near-ground air temperatures ranged between −0.2° and 0.5°C, with wet-bulb temperatures always below 0°C due to relative humidity around 90%. This event is therefore a perfect showcase for the objectives of the campaign: precipitation was sampled in near-melting conditions with the top of the melting layer roughly at the ground level, where the MASC occasionally captured images of melting snowflakes (Figs. 4 and 9).

Figure 7 provides entire time series of several ground radar products during the time of the ATR-42 flight, whereas Fig. 8 highlights airborne and ground-based observations during about 5–10 min corresponding to one single flight leg performed just before 1430 UTC.

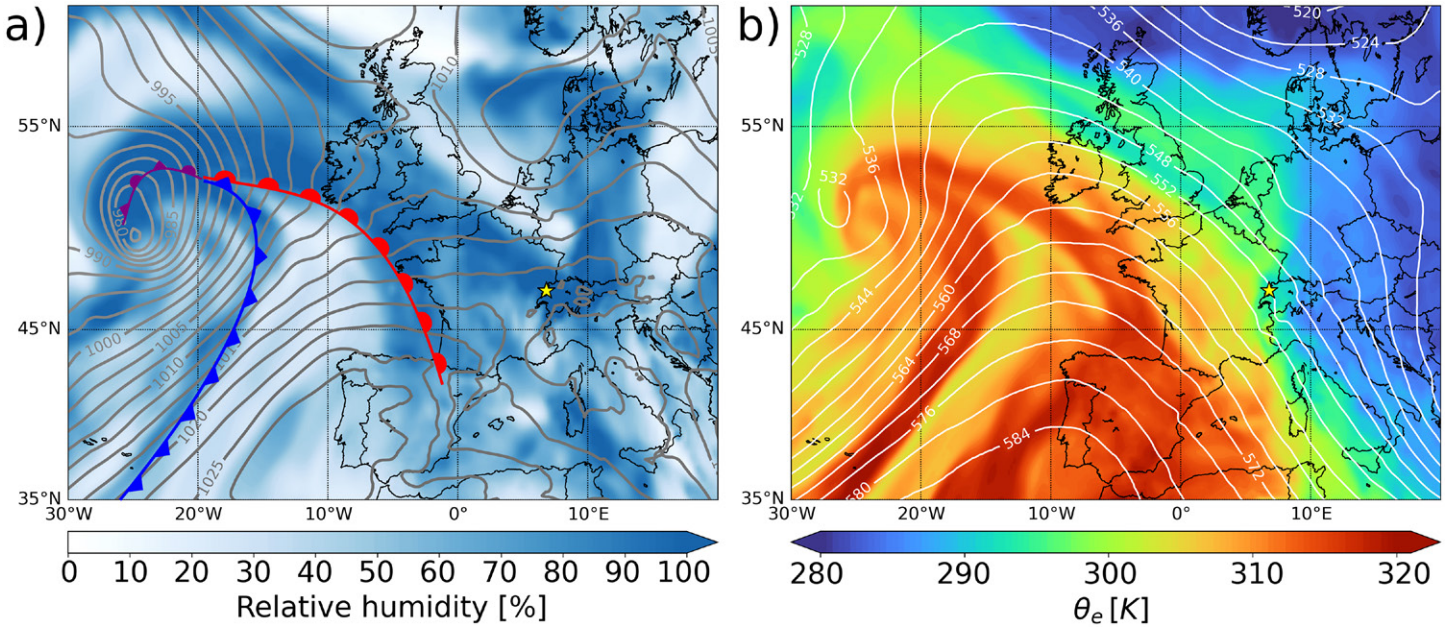

Fig. 6. Synoptic map at 1200 UTC 27 Jan from ERA5 data. (a) Relative humidity at 700 hPa (shading) and mean sea level pressure (contours; units: hPa). The blue, red, and purple lines represent the cold, warm, and occluded fronts, respectively (analysis based on 850 hPa temperature, mean sea level pressure, and satellite images). (b) Equivalent potential temperature at 850 hPa (shading) and geopotential height at 500 hPa (contours; units: dam). The yellow stars indicate the location of La Chaux-de-Fonds.

Cloud signatures in the radar data (Figs. 7a,b) indicate the presence of several cloud layers, with high-level clouds (6–8 km above ground) above lower layers extending to 3–5 km above ground, visible, for instance, between 1430 and 1530 UTC. Active generating cells can be observed in the W-band data between 3 and 5 km, especially after 1500 UTC.

The PIP-based classification of hydrometeor types, for particles with $D_{max} > 2$ mm (Jaffeux et al. 2022), indicates the dominant particle type to be aggregates (rimed: 29% and fragile: 24%), followed by columnar crystals (20%) and graupel (20%), over the 97,836 nontruncated particles in that size range sampled during the legs of this flight. The 2D-S classification of small particles ($D_{max} < 1.28$ mm, cf. Fig. 5) reveals a dominant presence of columnar crystals in the region 2–3 km MSL, i.e., 1–2 km above ground; the temperature range in this region is within that of columnar crystal growth and presumably secondary ice production (–10° to –3°C; e.g., Hallett et al. 1958), which suggests that ice production and growth by vapor deposition are occurring at those altitudes. The median mass diameter (MMD, derived from 2D-S and PIP measurements, cf. Fig. 5), a statistical indicator of the particles mass-weighted size, which is particularly relevant for aircraft industry applications (e.g., Leroy et al. 2016), was between 1 and 3 mm during this flight, with maximum values up to 5 mm.

Insights from complementary measurements. Figures 7–9 illustrate the complementarity of the joint airborne and ground-based, remote sensing and in situ measurements. In Fig. 7, precipitation processes are illustrated using different ground instruments: the high-sensitivity W-band profiler (WProf) allows for measurements up to cloud tops (~9.6 km MSL), and it is complemented by X-band data. The added value of multifrequency radar measurements is well established for the study of snowfall properties and processes [e.g., Matrosov (1998), Kneifel et al. (2015), and Mróz et al. (2021), to list a few]: they leverage the fact that snow particles, as they grow, transition to non-Rayleigh scattering regimes at short wavelengths (e.g., W band), while they essentially remain Rayleigh scatterers for larger wavelengths (e.g., X band). Increasing values of dual-frequency reflectivity (DFR) ratio, resulting from a complex interplay of microphysical processes (Mason et al. 2019), typically reveal the

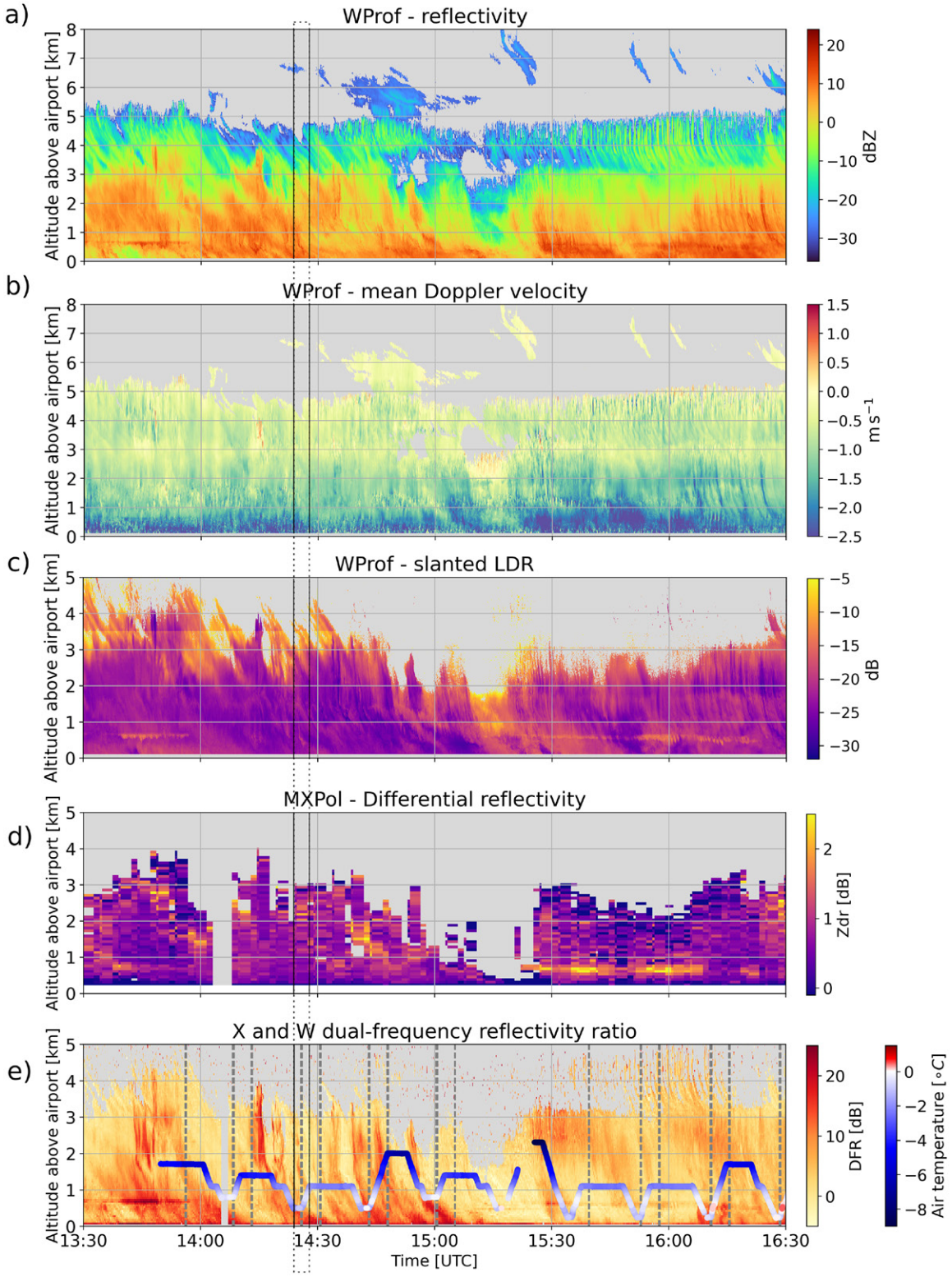

Fig. 7. Time series of radar data during the ATR-42 flight at 1330–1630 UTC 27 Jan. The three top panels display WProf zenith measurements: (a) radar reflectivity Ze, (b) mean Doppler velocity (with the convention that downward velocities are negative), and (c) slanted linear depolarization ratio. (d) Z_{DR} measured by MXPol (the RHIs are remapped to a Cartesian grid and vertical profiles are extracted at a horizontal distance corresponding to the location of the airport (±250m), using only elevations below 45°). (e) Dual-frequency reflectivity ratio, derived from ROXI and WProf data (DFR = Ze_x – Ze_w, in logarithmic units); the aircraft trajectory is overlaid, color-coded with the air temperature measured by the aircraft; dashed lines indicate time steps of aircraft overpasses. In all panels, vertical lines indicate the time frame (1419–1427 UTC) of Fig. 8.

growth, within the particle size distribution, in particle size, mass, and/or density (Liao et al. 2016), as visible in the time series of Fig. 7e at 1345 UTC (2–3 km MSL), 1415 UTC (2–3 km MSL), and 1450 UTC (1–2 km MSL) with DFR > 15 dB. It should be noted that radar measurements (especially at W band) can be affected by attenuation, resulting from the presence of wet—and to a lesser extent, dry—snow, of supercooled liquid water, or of water vapor (e.g., Kneifel et al. 2015; Protat et al. 2019), as well as from the presence of liquid water on the antenna or radome of certain radars.[4] Without correction, quantitative analyses of the dual-frequency reflectivity ratio should be conducted with care. A qualitative interpretation of spatiotemporal features, such as the fall streaks mentioned earlier, remains however relevant. Here, these regions also feature relatively low (~−28 dB) slanted linear depolarization ratio (LDR, Fig. 7c), which are compatible with riming or aggregation processes, while higher slanted LDR values (~−12 dB) sometimes seen near cloud top could be interpreted as a signature of columnar crystals. Combining observations of reflectivity-based variables to mean Doppler velocity allows to further refine the identification of snowfall growth mechanisms (e.g., Mason et al. 2018; Oue et al. 2021): for instance, the fall streak extending from 1 to 3 km around 1435 UTC displays relatively high DFR (~8 dB) and low slanted LDR (~−25 dB), together with a large mean Doppler velocity (~−1.5 m s^{-1}), which could indicate a riming occurrence. In situ observations and Doppler spectra collected (not shown here) support this hypothesis.

[4] This is not the case for WProf, which is equipped with blowers (Küchler et al. 2017).

Another noticeable feature is the bright band around 600–800 m above ground, visible in reflectivity (Ze), slanted LDR, DFR, and Z_{DR} between 1330 and 1400 UTC, and from 1530 to 1630 UTC. Airborne temperature data—color coded on the aircraft trajectory in Fig. 7e; see also Fig. A1—confirm the presence of temperature inversion, leading to near-zero temperatures both near ground and in the layer of enhanced reflectivity. This bright band is therefore the signature of a partial melting layer whereby an air parcel with positive temperatures—resulting from the warm-front arrival—is overlying a colder region where the partially melted hydrometeors

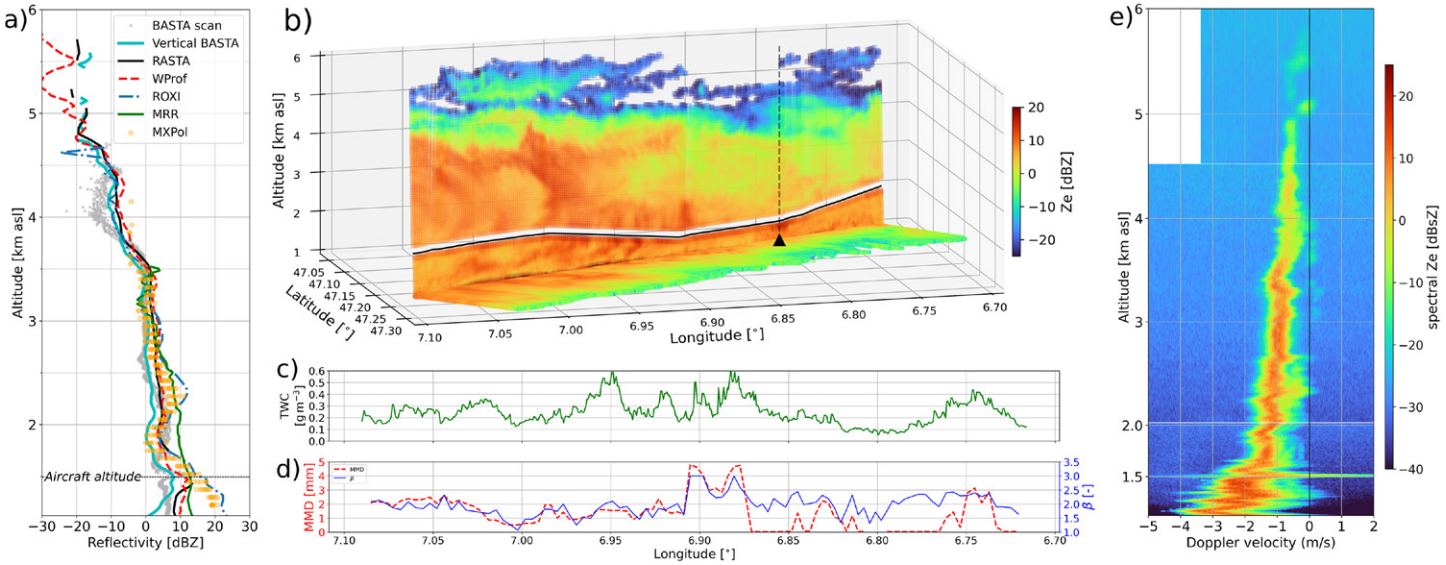

Fig. 8. Overview of an aircraft overpass of the measurement site from ground-based and airborne data sources. (a) Vertical profiles of equivalent reflectivity (Ze) collected by multiple data sources (ground-based and airborne radars) between 1425 and 1426 UTC. (b) Flight path (1419–1427 UTC) of the ATR-42 with airborne RASTA Ze; airborne BASTA Ze in the horizontal plane is also shown (projection to ground level for visualization purposes). The location of the ground-based instruments is indicated by a black triangular marker. (c) Time series of the TWC sampled by the CVI; (d) MMD and mass–size exponent β retrieved from 2D-S and PIP (Leroy et al. 2016). (e) Example of a Doppler reflectivity spectrum collected by WProf at the same time step {unit: 1 dBsZ = 10log$_{10}$[1 mm^6 m^{-1} (m s^{-1})$^{-1}$]}; the broad spectrum around 1.5 km MSL is caused by the wake of the aircraft; the missing data above 4.5 km is due to the smaller Nyquist velocity in this chirp.

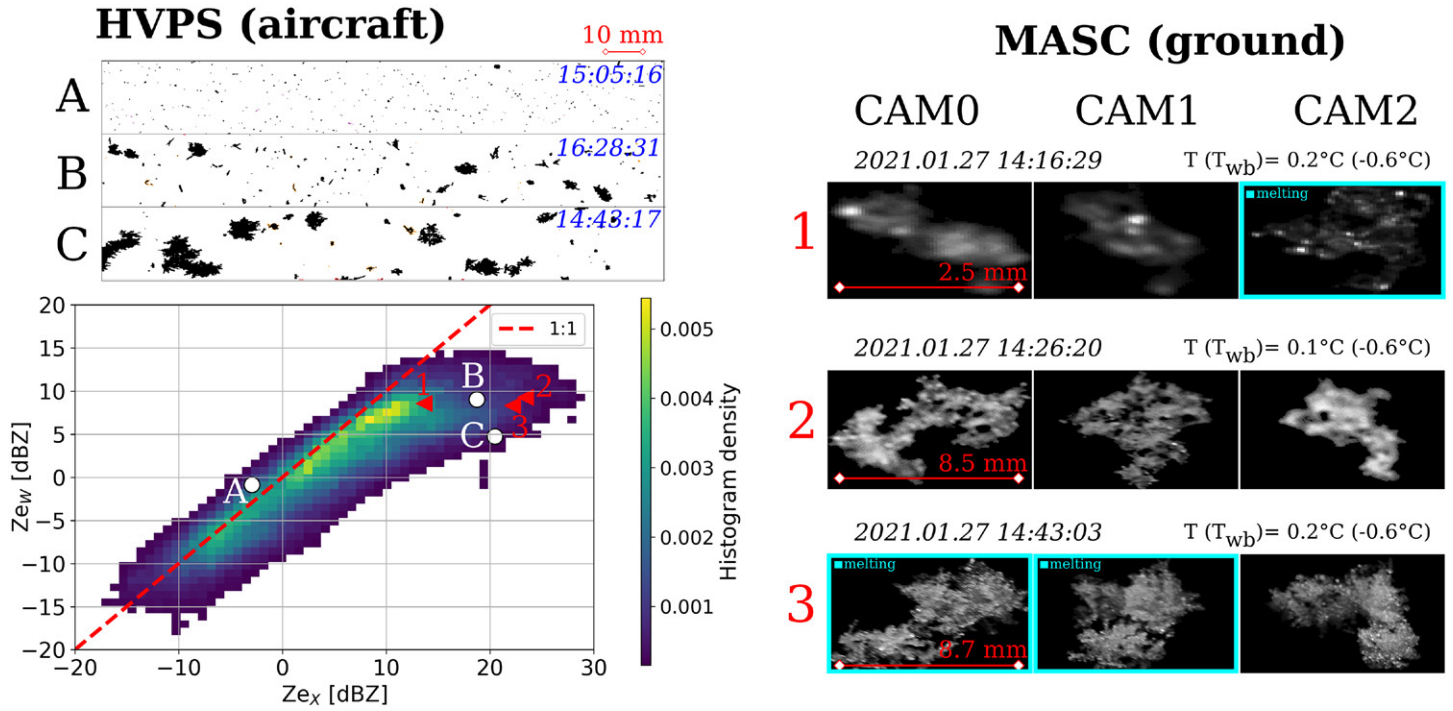

Fig. 9. (bottom left) Scatterplot, displayed as 2D histogram density, of X- and W-band collocated Ze observed by ROXI and WProf, respectively. The color-coded density data cover the entire time frame of the aircraft flight presented in Fig. 7. (right) MASC image triplets collected at ground level at three different time steps are shown , as well as information about near-ground temperature and wet-bulb temperature. Particles identified as melting by the method of Praz et al. (2017) are highlighted with a cyan frame. (top left) A few HVPS images are shown, for time steps at which the aircraft was within 250 m horizontal distance with respect to the radars. The MASC and HVPS images are contextualized to points of the scatterplot by extracting the X- and W-band reflectivity at the nearest valid (time, range) gate: for the MASC (red triangles), this corresponds to the third radar gate (150 m above ground); for the HVPS (white circles), this corresponds to the altitude of the aircraft above ground.

freeze again. This refreezing process may be partly responsible for the enhanced Doppler velocities observed below these layers, which are characteristic of dense, fast-falling particles.

The detailed spatiotemporal structure of precipitation can be visualized as illustrated in Fig. 8, focusing on a shorter time frame during an overpass of the aircraft on the instrumented site. Reflectivity measurements from the airborne RASTA (vertical profiles) and BASTA (horizontal profiles) radars are shown on the same image (Fig. 8b). In situ measurements of TWC along the aircraft trajectory, displayed in Fig. 8c, qualitatively match expected behaviors: larger TWC values are observed when the aircraft crosses regions with enhanced radar reflectivity. Comparing TWC to the retrievals of MMD and exponent of the mass–size relation [$m = \alpha D^{\beta}$, with α and β retrieved from 2D-S and PIP probes and an integrated mass constraint from the TWC, following Leroy et al. (2016)], in Fig. 8d, brings additional information about how the mass is distributed over the population of particles as well as some indications on active microphysical processes. For instance, aggregation can increase MMD and riming can increase β from typical values around 2 to values almost reaching 3. The inspection, visual or automatic, of actual hydrometeor images eventually allows us to back up these interpretations case by case. Note that the calculated β exponent (Leroy et al. 2016) is just a time-dependent value, retrieved from 2D-S and PIP image analysis for all particle sizes and for any heterogeneous mixture of size dependent particle morphologies observed during each second of the flight. Exceptionally low β values were retrieved when approaching longitude close to 7° (Fig. 8d), with increasing 2D-S concentrations of numerous elongated columns and simultaneous decrease in PIP large particle concentrations, giving significant weight to β value from the observed columns in the 2D-S images. Some understanding of the larger-scale spatiotemporal precipitation structures can be gained when complementing

these observations with a PPI of the operational radar in Montancy, as shown in Fig. A2. The reflectivity profiles of all radars at the time step of the overpass are displayed in Fig. 8a. The ground-based profilers (X and W band) and airborne (RASTA) radars were cross calibrated, relying on the mini-BASTA as a reference [which had absolute calibration following Toledo et al. (2020)]. This calibration transfer was performed using a set of cloud profiles carefully selected to avoid disparities caused by differences in sensitivity or scattering regime [research on this topic is ongoing, following the work of Toledo Bittner (2021)]. In the case of cross calibration of the RASTA radar, the profiles were selected from time steps when the aircraft overpasses the ground site.

Doppler spectra, as shown on Fig. 8e (same time step), reveal additional features such as secondary modes in the particle size distributions (here between 2 and 2.7 km MSL, and between 3 and 4 km MSL), indicative of the coexistence of different hydrometeor populations within the same radar resolution volumes.

In Fig. 9, we take a closer look at pictures from airborne (HVPS) and ground-based (MASC) imagers, relating them to remote sensing measurements. The (Ze_X, Ze_W) scatterplot illustrates the deviation from the Rayleigh scattering regime at W band for high reflectivities, associated with large particles—here again, a quantitative interpretation is delicate in the absence of attenuation correction. HVPS and MASC images from a few time steps are matched to points of the (Ze_X, Ze_W) scatterplot: it is noteworthy that aggregates with maximum dimension of about 1 cm (red markers labeled as 2 and 3) are observed by the MASC at time steps with high reflectivity and high dual-frequency ratio close to the ground; similarly, small particles visible in HVPS correspond to low DFR (point A), and increasingly bigger aggregates to larger DFR (B and C). This should, of course, be handled with care, since the radar moments reveal information on statistical distributions corresponding to much larger volumes than the sampling of the HVPS or the MASC. It nevertheless nicely illustrates the added value of the dataset: detailed in situ information is available and collocated to remote sensing measurements.

Summary and future work

The measurements conducted during the field campaign described in this paper aim to give momentum to snowfall microphysics research focused on processes and properties at temperatures ranging from −10° to +2°C. The combination of remote sensing, in situ, and aircraft-based measurement techniques was designed to sample clouds and precipitation through the entire column and at different scales, from the large sampling volumes of radar data to the depiction of individual hydrometeors of imagers. The experimental setup and aircraft sampling strategy were designed to maximize the overpasses above the ground site and hence the joint in situ and remote sensing measurements. This paper provides a detailed overview of the field experiment and a few examples of preliminary analyses.

The examples shown in the paper were selected to demonstrate the potential of the dataset. Data will be used to answer specific technical questions coming from the aviation sector: statistics of detailed microphysical snow properties (mass–size relation, morphological class, dry or wet snow, crystal density, sphericity, etc.) at the given temperatures are needed as fundamental input for accretion simulations and laboratory experiments. At the same time, underlying scientific questions will be investigated. The setup is ideal to improve existing or develop new retrievals of snowfall rate and snowfall microphysics from remote sensing observations (at single or multiple frequencies and polarization), and to validate those with in situ observations, with reuse potential for satellite-based products. The collocated polarimetric measurements and multifrequency Doppler spectral profiles can be jointly used for process-oriented analyses.

The dataset also opens up possibilities to investigate the melting layer in terms of microphysical processes and electromagnetic/attenuation properties, by means of radar and

in situ observations (including joint analysis of geometrical properties at the scale of individual particles and bulk water or ice content measurements) collected quasi-simultaneously above, below, and within the melting region.

The abundance of in situ data provides ground truth for hydrometeor classification algorithms based on remotely sensed observations (e.g., Besic et al. 2018). This is of particular interest to operational weather services with the presence of the Montancy radar of Météo-France at close range. Investigations in this direction have already started.

The data will be important in the field of numerical weather prediction, for example, for the improvement and validation of microphysical schemes in meteorological models, through the comparison of model outputs with in situ measurements or radar retrievals in a region of complex orography.

The measurement campaign is a milestone in the broader context of ICE GENESIS. It will support the parameterization of snowfall thermo- and aerodynamic models and the simulations of snow accretion performed by other working groups within the project, with the long-term goal being, as a bridge between research and industrial needs, to use the retrieved microphysical properties to develop engineering tools and de-risk system design early in the development process.

Acknowledgments. This project has received support from the European Union's Horizon 2020 research and innovation programme under Grant Agreement 824310 (ICE GENESIS project). Jacopo Grazioli received financial support from the Swiss National Science Foundation (Grant 175700/1). We thank MeteoSwiss for data availability and the possibility to install the MASC within a measurement site. We are grateful to Radiometer Physics GmbH for their help in having an operative radar system (WProf) during the campaign. EPFL-LTE acknowledges the help of Michael Monnet and Stéphanie Beaufils during preparation, installation, and maintenance of the instruments. Airborne data were obtained using the aircraft managed by SAFIRE, the French facility for airborne research, an infrastructure of the French National Center for Scientific Research (CNRS), Météo-France and the French National Center for Space Studies (CNES). Most of the microphysical in-situ data were collected using instruments (CDP-2, 2D-S, PIP, HVPS, CVI-snow, ROBUST) from the French Airborne Measurement Platform, a facility partially funded by CNRS/INSU and CNES. We are grateful to Les Éplatures airport, and in particular to Mr. Philippe Clapasson, for allowing the installation of the ground radars within a parking area at the airport, and for helping in the deployment of the instruments. We also thank the Dijon airport staff for their support when the ATR42 was stationed there.

Data availability statement. The data are available on the *Aeris* platform (https://ice-genesis.aeris-data.fr/catalogue/).

Appendix: Complementary information

Table A1 provides additional technical characteristics of the various radar systems in order to clearly illustrate the different resolutions, sensitivities, and beam widths.

Figure A1 illustrates the evolution of the temperature profile sampled by the aircraft with time. A near-ground temperature inversion is visible in the profiles and the 0°C temperature is sometimes crossed twice over the same profile. The inversion can be explained by the presence of a warmer air mass aloft, which settles in as the warm front passes.

Figure A2 shows the larger-scale coverage of a nearby-located operational radar; also, large-scale radar data were available for future comparisons with airborne instruments.

Table A1. Properties and parameters of the ground-based and airborne radars. Note that WProf uses three chirps, whose ranges are as follows: chirp 0, 104–998 m; chirp 1, 1,008–3,496 m; chirp 2, 3,512–8,683 m. When applicable, the properties for each chirp are separated by a slash. BASTA-mobile and mini-BASTA operate three modes (sequentially) with varying range resolutions; each of these modes is detailed in a separate line of the table.

Name	Frequency (GHz)	Transmission	3 dB beamwidth (°)	Sensitivity at 2 km range (dB*Z*)	Time resolution (s)	Range resolution (m)	Nyquist velocity (m s^{-1})
WProf	94	FMCW	0.53	–41	5	7.5/16/32	10.8/6.92/3.3
MRR	24	FMCW	1.5	–9	30	20	6
ROXI	9.48	Pulsed	1.8	–19	5	50	11
BASTA-mobile (12.5 m)	94.68	FMCW	0.4	–38	1	12.5	10
BASTA-mobile (25 m)	—	—	—	–42	—	25	5
BASTA-mobile (100 m)	—	—	—	–44	—	100	5
Mini-BASTA (12.5 m)	95.82	FMCW	0.8	–34	1	12.5	10
Mini-BASTA (25 m)	—	—	—	–37	—	25	5
Mini-BASTA (100 m)	—	—	—	–40	—	100	5
MXPol	9.41	Pulsed	1.3	–18	5 min scan cycle	75	39/7.96
Airborne BASTA	94.56	FMCW	0.9	–15.5/–22	0.5/1	12.5/25	10/10
Airborne RASTA	94.95	Pulsed	0.8	–28	0.5	30	15.8

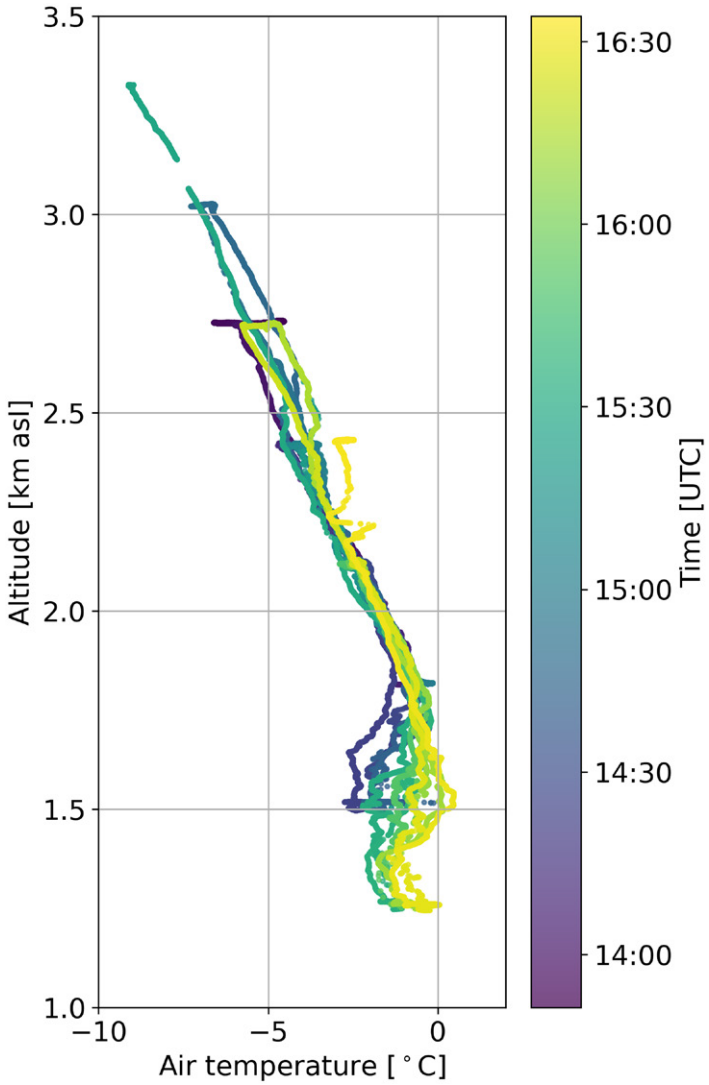

Fig. A1. Air temperature sampled by the aircraft on the flight of 27 Jan 2022 as a function of altitude. Time is color coded.

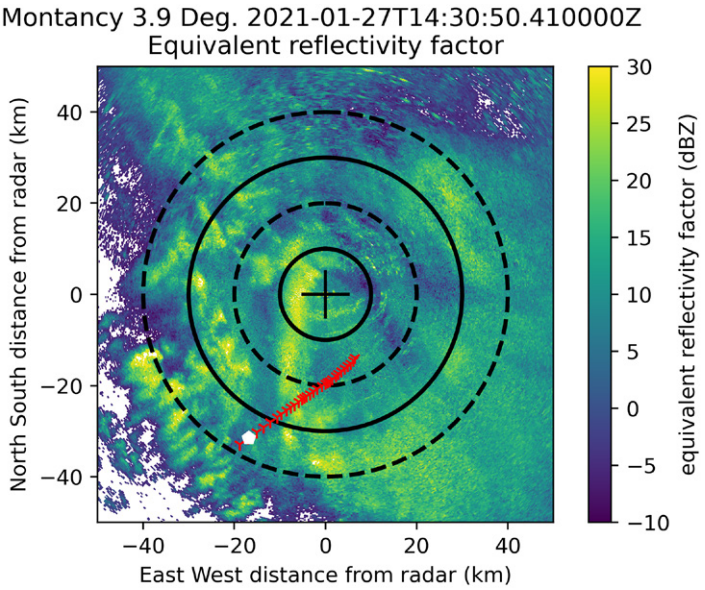

Fig. A2. Plan position indicator (PPI) of radar reflectivity collected by the operational radar of Montancy, France, around the time of the measurements shown in Fig. 8. A white marker indicates the location of the ground-based instruments of the campaign, while the red path is the aircraft trajectory in this time step. Circles are drawn at 10 km range distances from the radar location.

References

Aguilar, B., and Coauthors, 2021: Experimental and numerical investigations of snow accretion. *AIAA Aviation Forum 2021*, Online, American Institute of Aeronautics and Astronautics, AIAA 2021-2684, https://doi.org/10.2514/6.2021-2684.

Anderson, T. L., D. S. Covert, and R. J. Charlson, 1994: Cloud droplet number studies with a counterflow virtual impactor. *J. Geophys. Res.*, **99**, 8249, https://doi.org/10.1029/93JD03522.

Barthazy, E., W. Henrich, and A. Waldvogel, 1998: Size distribution of hydrometeors through the melting layer. *Atmos. Res.*, **47–48**, 193–208, https://doi.org/10.1016/S0169-8095(98)00065-9.

Baumgardner, D., and Coauthors, 2017: Cloud ice properties: In situ measurement challenges. *Ice Formation and Evolution in Clouds and Precipitation: Measurement and Modeling Challenges*, *Meteor. Monogr.*, No. 58, Amer. Meteor. Soc., https://doi.org/10.1175/AMSMONOGRAPHS-D-16-0011.1.

Bellon, A., I. Zawadzki, and F. Fabry, 1997: Measurements of melting layer attenuation at X-band frequencies. *Eur. J. Radiol.*, **32**, 943–955, https://doi.org/10.1029/97RS00492.

Besic, N., J. Gehring, C. Praz, J. Figueras i Ventura, J. Grazioli, M. Gabella, U. Germann, and A. Berne, 2018: Unraveling hydrometeor mixtures in polarimetric radar measurements. *Atmos. Meas. Tech.*, **11**, 4847–4866, https://doi.org/10.5194/amt-11-4847-2018.

Billault-Roux, A. C., and A. Berne, 2021: Integrated water vapor and liquid water path retrieval using a single-channel radiometer. *Atmos. Meas. Tech.*, **14**, 2749–2769, https://doi.org/10.5194/amt-14-2749-2021.

Bousquet, O., and Coauthors, 2015: Multifrequency radar observations collected in Southern France during HyMeX-SOP1. *Bull. Amer. Meteor. Soc.*, **96**, 267–282, https://doi.org/10.1175/BAMS-D-13-00076.1.

——, J. Delanoë, and S. Bielli, 2016: Evaluation of 3D wind observations inferred from the analysis of airborne and ground-based radars during HyMeX SOP-1. *Quart. J. Roy. Meteor. Soc.*, **142**, 86–94, https://doi.org/10.1002/qj.2710.

Cao, Y., W. Tan, and Z. Wu, 2018: Aircraft icing: An ongoing threat to aviation safety. *Aerosp. Sci. Technol.*, **75**, 353–385, https://doi.org/10.1016/j.ast.2017.12.028.

Chase, R. J., and Coauthors, 2018: Evaluation of triple-frequency radar retrieval of snowfall properties using coincident airborne in situ observations during OLYMPEX. *Geophys. Res. Lett.*, **45**, 5752–5760, https://doi.org/10.1029/2018GL077997.

Currier, W. R., T. Thorsona, and J. D. Lundquist, 2017: Independent evaluation of frozen precipitation from WRF and PRISM in the Olympic Mountains. *J. Hydrometeor.*, **18**, 2681–2703, https://doi.org/10.1175/JHM-D-17-0026.1.

Delanoë, J., A. Protat, O. Jourdan, J. Pelon, M. Papazzoni, R. Dupuy, J.-F. Gayet, and C. Jouan, 2013: Comparison of airborne in situ, airborne radar–lidar, and spaceborne radar–lidar retrievals of polar ice cloud properties sampled during the POLARCAT campaign. *J. Atmos. Oceanic Technol.*, **30**, 57–73, https://doi.org/10.1175/JTECH-D-11-00200.1.

——, and Coauthors, 2016: BASTA: A 95-GHz FMCW Doppler radar for cloud and fog studies. *J. Atmos. Oceanic Technol.*, **33**, 1023–1038, https://doi.org/10.1175/JTECH-D-15-0104.1.

Fabry, F., 1995: Long-term radar observations of the melting layer of precipitation and their interpretation. *J. Atmos. Sci.*, **52**, 838–851, https://doi.org/10.1175/1520-0469(1995)052<0838:LTROOT>2.0.CO;2.

Ferrone, A., and A. Berne, 2021: Dynamic differential reflectivity calibration using vertical profiles in rain and snow. *Remote Sens.*, **13**, 8, https://doi.org/10.3390/rs13010008.

——, A.-C. Billault-Roux, and A. Berne, 2022: ERUO: a spectral processing routine for the Micro Rain Radar PRO (MRR-PRO). *Atmos. Meas. Tech.*, **15**, 3569–3592, https://doi.org/10.5194/amt-15-3569-2022.

Field, P. R., and Coauthors, 2016: Secondary ice production - Current state of the science and recommendations for the future. *Ice Formation and Evolution in Clouds and Precipitation: Measurement and Modeling Challenges*, Meteor. Monogr., No. 58, Amer. Meteor. Soc., https://doi.org/10.1175/AMSMONOGRAPHS-D-16-0014.1.

Foresti, L., I. V. Sideris, L. Panziera, D. Nerini, and U. Germann, 2018: A 10-year radar-based analysis of orographic precipitation growth and decay patterns over the Swiss Alpine region. *Quart. J. Roy. Meteor. Soc.*, **144**, 2277–2301, https://doi.org/10.1002/qj.3364.

Garrett, T. J., C. Fallgatter, K. Shkurko, and D. Howlett, 2012: Fall speed measurement and high-resolution multi-angle photography of hydrometeors in free fall. *Atmos. Meas. Tech.*, **5**, 2625–2633, https://doi.org/10.5194/amt-5-2625-2012.

Grabowski, W. W., H. Morrison, S.-I. Shima, G. C. Abade, P. Dziekan, and H. Pawlowska, 2019: Modeling of cloud microphysics: Can we do better? *Bull. Amer. Meteor. Soc.*, **100**, 655–672, https://doi.org/10.1175/BAMS-D-18-0005.1.

Grandin, A., J.-M. Merle, M. Weber, J. Strapp, A. Protat, and P. King, 2014: AIRBUS flight tests in high total water content regions. *Sixth AIAA Atmospheric and Space Environments Conf.*, Atlanta, GA, American Institute of Aeronautics and Astronautics, AIAA 2014-2753, https://doi.org/10.2514/6.2014-2753.

Grazioli, J., G. Ghiggi, A.-C. Billault-Roux, and A. Berne, 2022: MASCDB, a database of images, descriptors and microphysical properties of individual snowflakes in free fall. *Sci. Data*, **9**, 186, https://doi.org/10.1038/s41597-022-01269-7.

Haggerty, J., and Coauthors, 2019: Detecting clouds associated with jet engine ice crystal icing. *Bull. Amer. Meteor. Soc.*, **100**, 31–40, https://doi.org/10.1175/BAMS-D-17-0252.1.

Hallet, J., and S. Mossop, 1974: Production of secondary ice particles during the riming process. *Nature*, **249**, 26–28, https://doi.org/10.1038/249026a0.

——, and G. A. Isaac, 2008: Aircraft icing in glaciated and mixed phase clouds. *J. Aircr.*, **45**, 2120–2130, https://doi.org/10.2514/1.37596.

——, B. J. Mason, and J. D. Bernal, 1958: The influence of temperature and supersaturation on the habit of ice crystals grown from the vapour. *Proc. Roy. Soc.*, **247A**, 440–453, https://doi.org/10.1098/rspa.1958.0199.

Hauk, T., E. Bonaccurso, P. Villedieu, and P. Trontin, 2016: Theoretical and experimental investigation of the melting process of ice particles. *J. Thermophys. Heat Trans.*, **30**, 946–954, https://doi.org/10.2514/1.T4886.

Heymsfield, A. J., A. Bansemer, M. R. Poellot, and N. Wood, 2015: Observations of ice microphysics through the melting layer. *J. Atmos. Sci.*, **72**, 2902–2928, https://doi.org/10.1175/JAS-D-14-0363.1.

Houze, R. A., and Coauthors, 2017: The Olympic Mountains Experiment (OLYMPEX). *Bull. Amer. Meteor. Soc.*, **98**, 2167–2188, https://doi.org/10.1175/BAMS-D-16-0182.1.

Jaffeux, L., A. Schwarzenböck, P. Coutris, and C. Duroure, 2022: Ice crystals images from optical array probes: Classification with convolutional neural networks. *Atmos. Meas. Tech.*, **15**, 5141–5157, https://doi.org/10.5194/amt-15-5141-2022.

Kneifel, S., A. Von Lerber, J. Tiira, D. Moisseev, P. Kollias, and J. Leinonen, 2015: Observed relations between snowfall microphysics and triple-frequency radar measurements. *J. Geophys. Res. Atmos.*, **120**, 6034–6055, https://doi.org/10.1002/2015JD023156.

Knight, C. A., 1979: Observations of the morphology of melting snow. *J. Atmos. Sci.*, **36**, 1123–1130, https://doi.org/10.1175/1520-0469(1979)036<1123:OOTMOM>2.0.CO;2.

Korolev, A., and T. Leisner, 2020: Review of experimental studies of secondary ice production. *Atmos. Chem. Phys.*, **20**, 11 767–11 797, https://doi.org/10.5194/acp-20-11767-2020.

——, and Coauthors, 2020: A new look at the environmental conditions favorable to secondary ice production. *Atmos. Chem. Phys.*, **20**, 1391–1429, https://doi.org/10.5194/acp-20-1391-2020.

Küchler, N., S. Kneifel, U. Löhnert, P. Kollias, H. Czekala, and T. Rose, 2017: A W-band radar–radiometer system for accurate and continuous monitoring of clouds and precipitation. *J. Atmos. Oceanic Technol.*, **34**, 2375–2392, https://doi.org/10.1175/JTECH-D-17-0019.1.

Lawson, R. P., L. J. Angus, and A. J. Heymsfield, 1998: Cloud particle measurements in thunderstorm anvils and possible weather threat to aviation. *J. Aircr.*, **35**, 113–121, https://doi.org/10.2514/2.2268.

Leinonen, J., and A. von Lerber, 2018: Snowflake melting simulation using smoothed particle hydrodynamics. *J. Geophys. Res. Atmos.*, **123**, 1811–1825, https://doi.org/10.1002/2017JD027909.

——, and Coauthors, 2018: Retrieval of snowflake microphysical properties from multifrequency radar observations. *Atmos. Meas. Tech.*, **11**, 5471–5488, https://doi.org/10.5194/amt-11-5471-2018.

Leroy, D., E. Fontaine, A. Schwarzenboeck, and J. W. Strapp, 2016: Ice crystal sizes in high ice water content clouds. Part I: On the computation of median mass diameter from in situ measurements. *J. Atmos. Oceanic Technol.*, **33**, 2461–2476, https://doi.org/10.1175/JTECH-D-15-0151.1.

Li, H., and D. Moisseev, 2019: Melting layer attenuation at Ka- and W-bands as derived from multifrequency radar Doppler spectra observations. *J. Geophys. Res. Atmos.*, **124**, 9520–9533, https://doi.org/10.1029/2019JD030316.

——, and ——, 2020: Two layers of melting ice particles within a single radar bright band: Interpretation and implications. *Geophys. Res. Lett.*, **47**, e2020GL087499, https://doi.org/10.1029/2020GL087499.

——, J. Tiira, A. Von Lerber, and D. Moisseev, 2020: Towards the connection between snow microphysics and melting layer: Insights from multifrequency and dual-polarization radar observations during BAECC. *Atmos. Chem. Phys.*, **20**, 9547–9562, https://doi.org/10.5194/acp-20-9547-2020.

Liao, L., R. Meneghini, L. Tian, and G. M. Heymsfield, 2009: Measurements and simulations of nadir-viewing radar returns from the melting layer at X and W bands. *J. Appl. Meteor. Climatol.*, **48**, 2215–2226, https://doi.org/10.1175/2009JAMC2033.1.

——, ——, A. Tokay, and L. F. Bliven, 2016: Retrieval of snow properties for Ku- and Ka-band dual-frequency radar. *J. Appl. Meteor. Climatol.*, **55**, 1845–1858, https://doi.org/10.1175/JAMC-D-15-0355.1.

Loeffler-Mang, M. L., M. Kunz, and W. Schmid, 1999: On the performance of a low-cost K-band Doppler radar for quantitative rain measurements. *J. Atmos. Oceanic Technol.*, **16**, 379–387, https://doi.org/10.1175/1520-0426(1999)016<0379:OTPOAL>2.0.CO;2.

Mariage, V., and Coauthors, 2017: IAOOS microlidar-on-buoy development and first atmospheric observations obtained during 2014 and 2015 Arctic drifts. *Opt. Express*, **25**, A73, https://doi.org/10.1364/OE.25.000A73.

Mason, J., W. Strapp, and P. Chow, 2006: The ice particle threat to engines in flight. *44th AIAA Aerospace Sciences Meeting and Exhibit*, Reno, NV, American Institute of Aeronautics and Astronautics, AIAA 2006-206, https://doi.org/10.2514/6.2006-206.

Mason, S. L., C. J. Chiu, R. J. Hogan, D. Moisseev, and S. Kneifel, 2018: Retrievals of riming and snow density from vertically pointing Doppler radars. *J. Geophys. Res. Atmos.*, **123**, 13 807–13 834, https://doi.org/10.1029/2018JD028603.

——, R. Hogan, C. Westbrook, S. Kneifel, and D. Moisseev, 2019: The importance of particle size distribution shape for triple-frequency radar retrievals of the morphology of snow. *Atmos. Meas. Tech.*, **12**, 4993–5018, https://doi.org/10.5194/amt-12-4993-2019.

Matrosov, S. Y., 1998: A dual-wavelength radar method to measure snowfall rate. *J. Appl. Meteor.*, **37**, 1510–1521, https://doi.org/10.1175/1520-0450(1998)037<1510:ADWRMT>2.0.CO;2.

McFarquhar, G. M., and Coauthors, 2017: Processing of ice cloud in situ data collected by bulk water, scattering, and imaging probes: Fundamentals, uncertainties, and efforts toward consistency. *Ice Formation and Evolution in Clouds and Precipitation: Measurement and Modeling Challenges, Meteor. Monogr.*, No. 58, Amer. Meteor. Soc., https://doi.org/10.1175/AMSMONOGRAPHS-D-16-0007.1.

McMurdie, L. A., and Coauthors, 2022: Chasing snowstorms: The Investigation of Microphysics and Precipitation for Atlantic Coast-Threatening Snowstorms (IMPACTS) campaign. *Bull. Amer. Meteor. Soc.*, **103**, E1243–E1269, https://doi.org/10.1175/BAMS-D-20-0246.1.

Mitra, S. K., O. Vohl, M. Ahr, and H. R. Pruppacher, 1990: A wind tunnel and theoretical study of the melting behavior of atmospheric ice particles. IV: Experiment and theory for snow flakes. *J. Atmos. Sci.*, **47**, 584–591, https://doi.org/10.1175/1520-0469(1990)047<0584:AWTATS>2.0.CO;2.

Morrison, H., and Coauthors, 2020: Confronting the challenge of modeling cloud and precipitation microphysics. *J. Adv. Model. Earth Syst.*, **68**, e2019MS001689, https://doi.org/10.1029/2019MS001689.

Mróz, K., A. Battaglia, S. Kneifel, L. von Terzi, M. Karrer, and D. Ori, 2021: Linking rain into ice microphysics across the melting layer in stratiform rain: A closure study. *Atmos. Meas. Tech.*, **14**, 511–529, https://doi.org/10.5194/amt-14-511-2021.

Murphy, A. M., A. Ryzhkov, and P. Zhang, 2020: Columnar Vertical Profile (CVP) methodology for validating polarimetric radar retrievals in ice using in situ aircraft measurements. *J. Atmos. Oceanic Technol.*, **37**, 1623–1642, https://doi.org/10.1175/JTECH-D-20-0011.1.

Oraltay, R. G., and J. Hallett, 2005: The melting layer: A laboratory investigation of ice particle melt and evaporation near 0°C. *J. Appl. Meteor. Climatol.*, **44**, 206–220, https://doi.org/10.1175/JAM2194.1.

Oue, M., P. Kollias, S. Y. Matrosov, A. Battaglia, and A. V. Ryzhkov, 2021: Analysis of the microphysical properties of snowfall using scanning polarimetric and vertically pointing multi-frequency Doppler radars. *Atmos. Meas. Tech.*, **14**, 4893–4913, https://doi.org/10.5194/amt-14-4893-2021.

Petäjä, T., and Coauthors, 2016: A field campaign to elucidate the impact of biogenic aerosols on clouds and climate. *Bull. Amer. Meteor. Soc.*, **97**, 1909–1928, https://doi.org/10.1175/BAMS-D-14-00199.1.

Plana-Fattori, A., A. Protat, and J. Delanoë, 2010: Observing ice clouds with a Doppler cloud radar. *C. R. Phys.*, **11**, 96–103, https://doi.org/10.1016/j.crhy.2009.11.004.

Poots, G., 2000: Introductory remarks (ice and snow accretion on structures). *Philos. Trans. Roy. Soc.*, **358**, 2803–2810, https://doi.org/10.1098/rsta.2000.0686.

Praz, C., Y.-A. Roulet, and A. Berne, 2017: Solid hydrometeor classification and riming degree estimation from pictures collected with a multi-angle snowflake camera. *Atmos. Meas. Tech.*, **10**, 1335–1357, https://doi.org/10.5194/amt-10-1335-2017.

Protat, A., J. Delanoë, D. Bouniol, A. J. Heymsfield, A. Bansemer, and P. Brown, 2007: Evaluation of ice water content retrievals from cloud radar reflectivity and temperature using a large airborne in situ microphysical database. *J. Appl. Meteor. Climatol.*, **46**, 557–572, https://doi.org/10.1175/JAM2488.1.

——, S. Rauniyar, J. Delanoë, E. Fontaine, and A. Schwarzenboeck, 2019: W-band (95 GHz) radar attenuation in tropical stratiform ice anvils. *J. Atmos. Oceanic Technol.*, **36**, 1463–1476, https://doi.org/10.1175/JTECH-D-18-0154.1.

Pruppacher, H., and J. Klett, 2010: Collision, coalescence, and breakup. *Microphysics of Clouds and Precipitation*, 2nd ed. L. Mysak and K. Hamilton, Eds., Springer, 568–616, https://doi.org/10.1007/978-0-306-48100-0.

Ramelli, F., and Coauthors, 2021: Microphysical investigation of the seeder and feeder region of an Alpine mixed-phase cloud. *Atmos. Chem. Phys.*, **21**, 6681–6706, https://doi.org/10.5194/acp-21-6681-2021.

Rasmussen, R., and Coauthors, 2001: Weather Support to Deicing Decision Making (WSDDM): A winter weather nowcasting system. *Bull. Amer. Meteor. Soc.*, **82**, 579–595, https://doi.org/10.1175/1520-0477(2001)082<0579:WSTDDM>2.3.CO;2.

——, J. Cole, R. K. Moore, and M. Kuperman, 2000: Common snowfall conditions associated with aircraft takeoff accidents. *J. Aircr.*, **37**, 110–116, https://doi.org/10.2514/2.2568.

Rasmussen, R. M., J. Vivekanandan, J. Cole, B. Myers, and C. Masters, 1999: The estimation of snowfall rate using visibility. *J. Appl. Meteor.*, **38**, 1542–1563, https://doi.org/10.1175/1520-0450(1999)038<1542:TEOSRU>2.0.CO;2.

Schneebeli, M., N. Dawes, M. Lehning, and A. Berne, 2013: High-resolution vertical profiles of X-band polarimetric radar observables during snowfall in the Swiss Alps. *J. Appl. Meteor. Climatol.*, **52**, 378–394, https://doi.org/10.1175/JAMC-D-12-015.1.

——, J. Grazioli, and A. Berne, 2014: Improved estimation of the specific differential phase shift using a compilation of Kalman filter ensembles. *IEEE Trans. Geosci. Remote Sens.*, **52**, 5137–5149, https://doi.org/10.1109/TGRS.2013.2287017.

Schwarzenbo, A., and J. Heintzenberg, 2000: Cut size minimization and cloud element break-up in a ground-based CVI. *J. Aerosol Sci.*, **31**, 477–489, https://doi.org/10.1016/S0021-8502(99)00535-2.

Skofronick-Jackson, G., and Coauthors, 2015: Global Precipitation Measurement Cold Season Precipitation Experiment (GCPEX): For measurement's sake, let it snow. *Bull. Amer. Meteor. Soc.*, **96**, 1719–1741, https://doi.org/10.1175/BAMS-D-13-00262.1.

Stewart, R. E., J. M. Thériault, and W. Henson, 2015: On the characteristics of and processes producing winter precipitation types near 0°. *Bull. Amer. Meteor. Soc.*, **96**, 623–639, https://doi.org/10.1175/BAMS-D-14-00032.1.

Strapp, J., J. D. MacLeod, and L. E. Lilie, 2008: Calibration of ice water content in a wind tunnel/engine test cell facility. *Extended Abstracts, 15th Int. Conf. on Clouds and Precipitation*, Cancun, Mexico, International Commission on Clouds and Precipitation, P13.1, http://cabernet.atmosfcu.unam.mx/ICCP-2008/abstracts/Program_on_line/Poster_13/StrappEtAl-extended.pdf.

Szyrmer, W., and I. Zawadzki, 1999: Modeling of the melting layer. Part I: Dynamics and microphysics. *J. Atmos. Sci.*, **56**, 3573–3592, https://doi.org/10.1175/1520-0469(1999)056<3573:MOTMLP>2.0.CO;2.

Taszarek, M., S. Kendzierski, and N. Pilguj, 2020: Hazardous weather affecting European airports: Climatological estimates of situations with limited visibility, thunderstorm, low-level wind shear and snowfall from ERA5. *Wea. Climate Extremes*, **28**, 100243, https://doi.org/10.1016/j.wace.2020.100243.

Toledo, F., J. Delanoë, M. Haeffelin, J. C. Dupont, S. Jorquera, and C. Le Gac, 2020: Absolute calibration method for frequency-modulated continuous wave (FMCW) cloud radars based on corner reflectors. *Atmos. Meas. Tech.*, **13**, 6853–6875, https://doi.org/10.5194/amt-13-6853-2020.

Toledo Bittner, F., 2021: Improvement of cloud radar products for fog surveillance networks: Fog life cycle analyses and calibration methodologies. Ph.D. thesis, Institut Polytechnique de Paris, 145 pp., https://tel.archives-ouvertes.fr/tel-03298445.

Trömel, S., A. V. Ryzhkov, B. Hickman, K. Mühlbauer, and C. Simmer, 2019: Polarimetric radar variables in the layers of melting and dendritic growth at X band—Implications for a nowcasting strategy in stratiform rain. *J. Appl. Meteor. Climatol.*, **58**, 2497–2522, https://doi.org/10.1175/JAMC-D-19-0056.1.

Vaillant De Guélis, T., A. Schwarzenböck, V. Shcherbakov, C. Gourbeyre, B. Laurent, R. Dupuy, P. Coutris, and C. Duroure, 2019: Study of the diffraction pattern of cloud particles and the respective responses of optical array probes. *Atmos. Meas. Tech.*, **12**, 2513–2529, https://doi.org/10.5194/amt-12-2513-2019.

Viltard, N., C. L. Gac, A. Martini, Y. Lemaître, N. Pauwels, J. Delanoë, and G. Lesage, 2019: Développements radar au LATMOS pour l'études des propriétés microphysiques des nuages et des précipitations. *ENVIREM 2019*, Palaiseau, France, HAL, 6 pp., https://hal.archives-ouvertes.fr/hal-02389653.

Wang, Z., and Coauthors, 2012: Single aircraft integration of remote sensing and in situ sampling for the study of cloud microphysics and dynamics. *Bull. Amer. Meteor. Soc.*, **93**, 653–668, https://doi.org/10.1175/BAMS-D-11-00044.1.